Int. J. Electrochem. Sci., 17 **(2022)** Article Number: 220844, doi: 10.20964/2022.08.38

International Journal of ELECTROCHEMICAL SCIENCE
www.electrochemsci.org

Experimental Study on the Electrochemical Properties and Matric Suction of Unsaturated Loess-like silt

Xinyu Liu, Pengju Han, Fuli Ma*, Bin He, Xiaoyuan Wang, Funan Sun, Zhiwei Chen, Xiangling Bai*

College of Civil Engineering, Taiyuan University of Technology, Taiyuan, 030024, China
*E-mail: 13834569544@163.com, mafuli@tyut.edu.cn

Received: 19 April 2022 / *Accepted:* 11 June 2022 / *Published:* 4 July 2022

The properties of unsaturated loess-like silt were explored by measuring the matric suction in the soil and recording electrochemical impedance spectra. Soil water characteristic curves were determined and equivalent circuits were integrated, which contain 7 purposeful resistance and reactance parameters. The matric suction and electrochemical characteristics of loess-like silt with different initial dry densities and water contents were studied. The relationship between them was then established. The results show that the dry density and water content of the soil have a significant effect on the matric suction and electrochemical characteristics of the loess-like silt. The electrochemical parameter pore resistance reflects the pore state of the soil and the connected pore resistance can characterize the strength of the matric suction in loess-like silt. The matric suction and connected pore resistance in loess-like silt with a given dry density are positively linearly correlated and the correlation increases or decreases as the water content is changed.

Keywords: Chilled-mirror dew-point meter, electrochemical impedance spectroscopy, matric suction, equivalent circuit.

1. INTRODUCTION

Loess is widely distributed around the world. The largest depositional area of loess occurs in China and covers approximately 640,000 km^2 [1, 2]. Its strata are continuous and complete which is rarely encountered in the world [3]. Externally, as a special kind of regional soil, loess is gray/yellow to brown/red in color. Internally, it features structures such as macropores and vertical joints [4] which affect the structural and dynamic characteristics of the loess as well as its water sensitivity [5].

With the introduction and implementation of China’s ‘One Belt, One Road’ construction policy (amongst others), more and more construction projects are passing through areas containing loess. In order to reduce the costs of such projects, the construction workers generally adopt the principle that local materials should be used. Thus, a large amount of loess and loess-like silt is being used as engineering fillers. However, loess-like silt is dominated by the silt particles present. These tend to have a single particle size, poor gradation, and their use can produce poor effects [6, 7]. Therefore, there is an important need for us to deepen our understanding of the engineering characteristics of loess to ensure that efficient and economic construction can continue in loess areas.

In nature, and in engineering practice, most natural soils are largely unsaturated [8]. The total suction in unsaturated soil consists of two parts: matric suction and osmotic suction [9]. Contemporary unsaturated soil mechanics regards the matric suction to be the difference between the stress in the outside and inside of the water–air interface (contraction film). It plays a key role in the links between various soil properties and the core reflecting the three-phases in the soil [5]. As such, it can be used to predict engineering properties such as soil strength [10].

The relationship between soil water content and matric suction can be plotted graphically in the form of a soil water characteristic curve (SWCC) [10]. Such curves describe the water-holding characteristics of the soil and play an important role in determining the mechanical behavior of unsaturated soil. They thus describe important relationships in the field of unsaturated soil mechanics [11]. Numerous scholars have studied the factors affecting matric suction and SWCCs, including the mineral composition of the soil, its pore structure, and temperature [12–16]. At the same time, other factors can also have indirect effects, e.g. the dry density, water content, and stress state of the soil [17–20]. Chen et al. [21], for example, pointed out that the dry density of the soil affects its SWCC because it affects the pore state of the soil.

There are many direct and indirect ways of measuring the total or matric suction in unsaturated soil. These include techniques employing filter paper measurements, pressure plate extractor measurements, vapor equilibrium measurements, tensiometers, chilled-mirror dew-point meter measurements, and so on [22–27]. However, most of these methods have serious shortcomings in terms of reliability, cost, application scope, and practicability [28]. Therefore, scholars in China (and elsewhere) have endeavored to predict matric suction values and SWCCs using other methods [29–31].

Unsaturated soil is a composite material composed of three-phases and can also be regarded as an electrochemical system. At present, electromagnetic techniques are widely used as such methods are non-destructive and can be rapidly applied, which shows their unique advantages. Electrochemical impedance spectroscopy (EIS), for example, is applied in the field of geotechnical engineering and can be used to study electric double-layers, electrode materials, corrosion and protection, etc. [32-39]. It is also widely used in the study of copper corrosion inhibitors [40-42], biosensing [43], lithium-ion battery modeling [44], and even applied to other fields such as food safety [45]. EIS uses a small-amplitude sinusoidal potential or current as a disturbance signal. The response of the system is measured and is often interpreted in the frequency domain. The dynamics of the system and the corresponding information about the structure of the electrode interface can thus be studied [33]. Scholars have used the technique to study the effects of mineral composition, temperature, dry density, water content, pH, ion concentration, and other factors on the electrochemical properties of soil. Results are combined with information about the microstructure of the soil to deduce the conductive path in the soil. Equivalent circuit models can then be established and used to analyze the significance of the various circuit elements to explore the internal structure of the soil [32–39]. However, research on the physical significance of specific elements is still incomplete.

In recent years, EIS has been applied more regularly to study the structural characteristics and physical and mechanical properties of soil [46]. For example, Wang et al. investigated the concept of solution resistance in the equivalent circuit model for silty clay [47]. They found that it can be used to determine the state of the pore water in the soil. The matric suction and electrochemical properties of loess-like silt are affected by its pore structure and other factors, including pore size, pore gradation, and composite structure.

In this paper, the results of chilled-mirror dew-point and electrochemical tests were combined with unsaturated soil mechanics and electrochemical theory to study the matric suction and electrochemical characteristics of loess-like silt. The physical significance of each parameter in the electrochemical equivalent circuit model was thus revealed. Mathematical relationships were also established between matric suction and the electrochemical parameters allowing the properties of the loess-like silt to be further explored.

2. TEST MATERIALS AND METHODS

The soil used in our experiments was obtained from a construction site in Dongshan, Taiyuan City, Shanxi Province, China. It is Q_4 loess and is yellow–brown in color. According to the report produced following a field investigation of the site, the dry density of the soil is about 1.4–1.65 $g \cdot cm^{-3}$. The basic physical properties of the soil are listed in Table 1 and the distribution of the sizes of the particles in the soil is shown in Fig. 1.

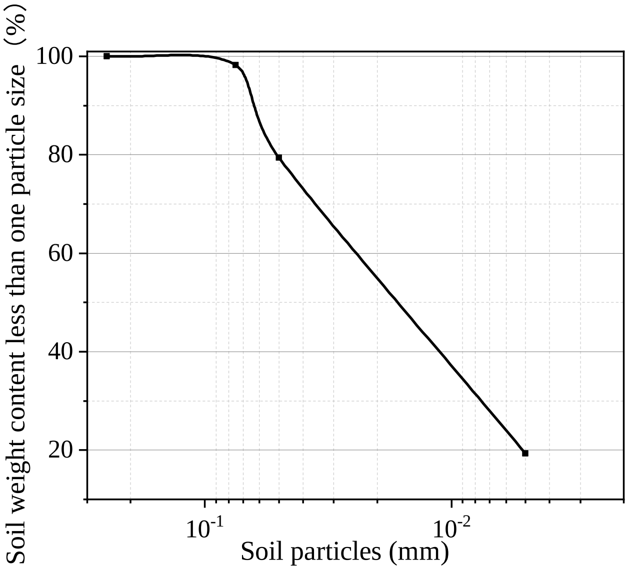

Figure 1. Distribution of the particle sizes in the soil.

Table 1. Basic physical properties of the soil.

Optimal water content %	Liquid limit %	Plastic limit %	Plasticity index	Specific gravity
15.30	25.25	15.61	9.6351	2.70

Overall, based on the abovementioned parameters, it is determined that the soil used is loess-like silt. X-ray diffraction (XRD) was further used to determine the mineral composition of the soil (Fig. 2). As can be seen, the soil mainly consists of quartz (40%), clay minerals (19.8%, mainly chlorite and illite), plagioclase (14.1%), and calcite (13.2%).

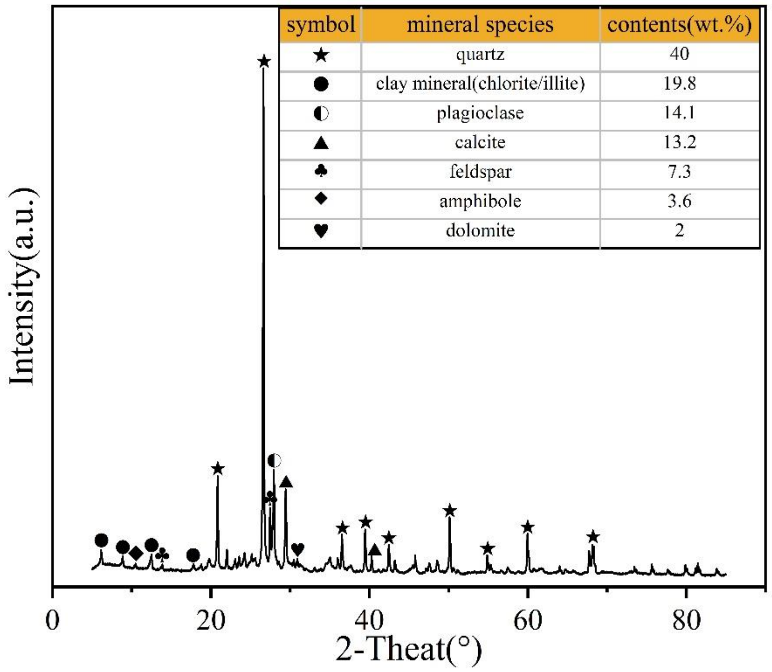

Figure 2. XRD pattern obtained using the soil.

2.2 Sample preparation

The soil was first allowed to dry naturally before being broken up and sieved (using a sieve with a mesh size of 1 mm). Samples were prepared with initial dry densities of 1.5 and 1.6 $g \cdot cm^{-3}$ and five different initial water contents (10%, 12%, 14%, 16%, and 18%). A test mold was prepared according to the size of the stainless steel sample cup used in the chilled-mirror dew-point meter (WP4C, METER), as shown in Fig. 3. Electrodes made of copper sheet also need to be attached to the upper and lower surfaces of the mold for use in the EIS tests.

In order to ensure the reliability of the test results, the required amount of dry soil and deionized water were calculated according to the mold volume and test scheme. Three identical soil samples were prepared for each of the 10 test groups (giving 30 soil samples in total). The soil samples were sealed and marked in turn. They were then tested after resting for 24 hours to allow the soil and water to become fully mixed.

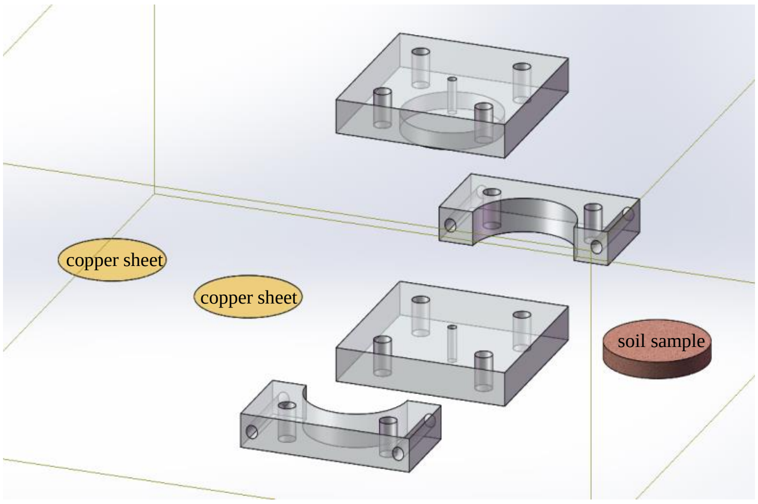

Figure 3. Schematic diagram of the mold used.

2.3 Matric suction tests

In these experiments, a conductivity meter (DDS-307A, INESA Scientific Instrument Co., Ltd.) and a chilled-mirror dew-point meter were used to measure the osmotic and total suction of the soil samples, respectively. The matric suction of the soil samples could then be calculated.

In the chilled-mirror dew-point meter, the space above the soil sample was allowed to equilibrate with the air in the sealed chamber. At equilibrium, the water potential of the air in the chamber was the same as that of the soil sample [48]. Measurements were recorded continuously over the range 0 to –300 MPa. The test was accurate to ±0.05 MPa and takes 15–30 min to perform. The chilled-mirror dew-point meter could only measure the total suction in the soil (i.e. sum of the matric and osmotic suction). Hence, it was necessary to use an electrical conductivity meter to measure the permeability suction of the test samples.

To determine the osmotic suction in the soil samples, a weighed sample of dry soil (20 g) was shaken with deionized water (100 ml) and allowed to equilibrate. The saturated solution above the soil was then extracted and transferred to a beaker. Its electrical conductivity was then determined.

To obtain the total suction in the soil, the soil sample was taken out from the mold and put into the stainless steel sample cup of the chilled-mirror dew-point meter (diameter 38 mm, height 10 mm). This was weighed and then placed in the sample chamber for direct measurement,as shown in Fig. 4. After the test, the sample cup was taken out and immediately weighed. It was then dried at 105 °C and weighed to calculate the actual water content. The osmotic suction and matric suction of the soil could then be found.

Figure 4. Soil samples in the stainless steel sample cup.

2.4 EIS tests

A three-electrode electrochemical workstation (CS-350, Corrtest Instruments Co., Ltd., Wuhan) was used to conduct the EIS tests on the soil samples. One of the copper electrodes in contact with the soil sample was used as the working electrode (WE); the one on the other side acted as the reference electrode (RE) and counter electrode (CE), as shown in Fig. 5. The AC tests were carried out at a temperature of 20 °C, each test lasted 5 minutes. The system was operated in impedance–frequency mode over a frequency range of 10^{-1}–10^{5} Hz. A linear logarithm scanning mode was employed.

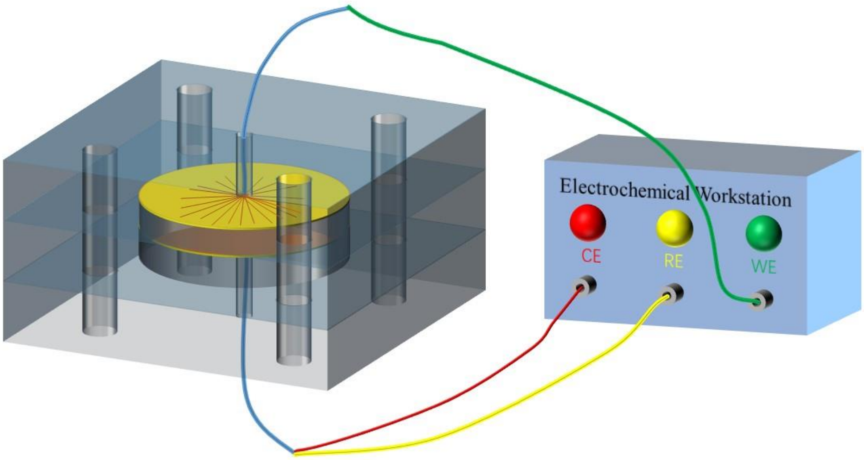

Figure 5. Electrochemical testing scheme.

The instrument can be used to directly obtain Nyquist and Bode diagrams for the soil samples. The Bode diagrams consist of two parts showing the variation of the modulus of the impedance (log|Z| vs. log$f$ diagram) and phase angle (θ vs. log$f$ diagram).

3. RESULTS AND DISCUSSION

3.1 Results of the suction tests and analysis

3.1.1 Results of the osmotic suction tests

Having prepared a saturated extract from a soil sample, the conductivity meter was used to measure the extract's electrical conductivity. The osmotic suction φ_{os} was then calculated using the expression:

$$\varphi_{os} = -0.036E_c \quad (1)$$

where E_c is the electrical conductivity of the soil. The values calculated using Eq. (1) are shown in Table 2.

Table 2. Osmotic suction of the saturated loess-like silt extracts.

E_c $\mu s/c$	$\overline{E_c}$ $\mu s/cm$	φ_{os} MPa
161.3 161.9 159.9	161.0	0.00005796

By measuring the actual water content of the soil samples in the later stage, the osmotic suctions of the soil samples with different dry densities and different water contents can be calculated using the expression:

$$\varphi = \varphi_{os}\frac{\theta_s}{\theta} \quad (2)$$

where θ is the volumetric water content and θ_s is the saturated value of the volumetric water content. The θ_s values of soil samples with dry densities of 1.5 and 1.6 $g \cdot cm^{-3}$ are found to be 44.45% and 40.74%, respectively.

3.1.2 Matric suction of the loessial silt samples

Loess-like silt samples with different dry densities and different water contents were prepared and the total suction in them was determined using the chilled-mirror dew-point meter. Eq. (2) was used to obtain the osmotic suction in the soil sample and then the matric suction in the soil sample was calculated. The resulting suction parameters are shown in Table 3.

Table 3. Suction parameters of the loess-like silt samples.

ρ_d g·cm^{-3}	Preset ω %	Box g	Box + Wet Soil g	Box + dry soil g	Actual ω %	Total suction MPa	Osmotic suction MPa	Matric suction Mpa
1.5	10	25.139	31.915	31.305	9.89	0.680	0.017	0.663
	12	24.979	31.880	31.168	11.50	0.400	0.015	0.385
	14	23.869	30.893	30.045	13.73	0.270	0.013	0.257
	16	25.219	32.369	31.419	15.32	0.230	0.011	0.219
	18	25.251	32.521	31.431	17.64	0.190	0.010	0.180
1.6	10	25.232	32.461	31.814	9.83	0.620	0.015	0.605
	12	25.219	32.579	31.815	11.58	0.360	0.013	0.347
	14	25.232	32.723	31.820	13.71	0.280	0.011	0.269
	16	24.979	32.602	31.570	15.66	0.240	0.010	0.231
	18	25.140	32.892	31.745	17.37	0.210	0.008	0.202

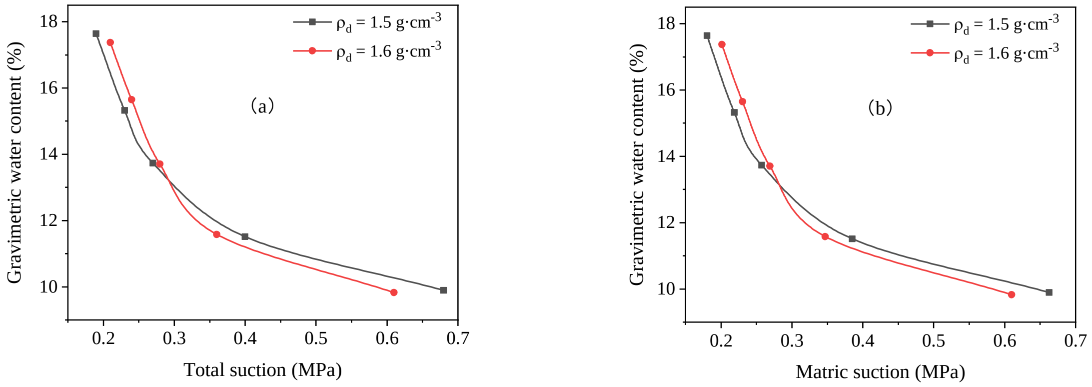

Figure 6. Variation of the total and matric suction in the loess-like silt with gravimetric water content.

Having determined the total suction, osmotic suction, and water content in loess-like silt samples with different dry densities and different water contents, the relationship between these variables can be presented graphically, as shown in Fig. 6. According to the conversion formula between volumetric and gravimetric water content, it can be seen that the variations of the two quantities are similar.

The results of the tests can also be fitted to the Van Genuchten model [49] which can be expressed mathematically in the form:

$$\theta_\omega = \theta_r + \frac{\theta_s - \theta_r}{[1+(\alpha\varphi)^q]^b} \qquad (3)$$

where θ_r is the residual volume water content, a denotes a model parameter related to the air-entry value, q is a model parameter related to pore size, and b is a model parameter related to the overall symmetry of the SWCC. The latter can either be considered to be such that $b = 1 - 1/q$ or a, q, and b can be taken to be independent of each other. When the a:b ratio is small, a is equal to the reciprocal of the air-entry value [50].

Table 4 and Fig. 7 show the results of the fitting process. The θ_r values of soil samples with dry densities of 1.5 and 1.6 g·cm^{-3} are 13.86% and 14.95%, respectively. After carrying out the necessary calculations, the air-entry values of the samples with dry densities of 1.5 and 1.6 g·cm^{-3} are found to be 0.13 and 0.18 MPa, respectively.

Table 4. Parameters derived by fitting the results to the Van Genuchten model.

ρ_d g·cm^{-3}	a	q	b	θ_s %	θ_r %	R^2
1.5	7.76	3.04	0.67	44.45	13.86	0.998
1.6	5.53	3.92	0.74	40.74	14.95	0.999

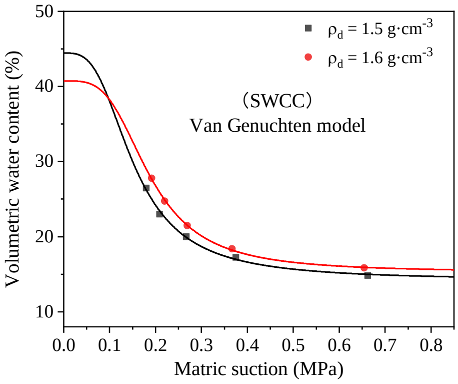

Figure 7. SWCC generated by fitting the data to the Van Genuchten model.

3.1.3 Analysis of the matric suction results

Fig. 6 shows that the water content has a significant effect on the total and matric suction in the soil. More specifically, the suction decreases monotonically as the water content increases over the range considered. When the water content is low, the total and matric suction values are large. Then, as the water content is increased, the total and matric suction values decrease rapidly at first and then more slowly. For a given dry density value, increasing the water content means an increase in saturation, and so the change in the total and matric suction with saturation is similar to the variation with water content [51].

It can also be seen from Fig. 6 that the total and matric suction are also affected by the dry density of the soil. When the water content is low, the suction in the soil sample with the higher dry density value is lower than that in the sample with the lower dry density value. When the water content is high, however, this order is reversed. The two curves can thus be seen to cross when the water content is ~13% and at this point the suction does not appear to change as the dry density of the sample varies.

Table 4 indicates that the data fit the Van Genuchten expression very well (the goodness-of-fit R^2 values exceed 99.7% for both of the dry density values used). Vanapali et al. [52] produced a modified physical model to account for the SWCC curve (according to the air-entry value) and divided it into three stages: a boundary effect stage, a transition stage, and a residual stage. As can be seen from Fig. 7, the SWCCs are relatively flat at both their ends (when the water content is close to the residual and boundary effect stages). In these regions, the matric suction changes very rapidly as the water content changes. In the transition stage, the rate of change is much slower (that is, the matric suction changes relatively slowly as the water content changes).

This behavior may arise because the water film around the soil particles experiences a strong binding effect when the volumetric water content is low or close to the residual water content. The pore connectivity of the soil structure is therefore much better, the water holding capacity of the soil is increased, and the matric suction will be sensitive to a change in water content. In addition, when the volumetric water content of the soil sample drops to the residual water content value, the matric suction will reach its maximum value. As the water content increases, the strength of the bonding between particles is weakened [53]. The size and connectivity between the pores inside the soil thus changes. This affects the area of the soil–water interaction and the shape of the contraction film [54]. The radius of curvature of the bending surface in the soil pores also decreases and the water-holding capacity of the soil decreases. This continues until the pores are gradually occupied and the soil reaches a state of saturation. At this point, the soil cannot adsorb any more water.

Therefore, the effect of water content on the SWCC can be expressed in terms of the change in the pore state of the soil. It can also be seen from Fig. 7 that the residual matric suction increases as the dry density of the soil increases. The saturated water content value also decreases as the dry density increases [21] and the air-entry value also increases [50]. A larger dry density value implies that there are fewer pores in the soil and that their volumes are smaller. This implies there is better contact between soil particles and the pore connectivity in the soil structure is relatively poor. Therefore, when the water content is close to the residual stage, the water between these soil particles will be difficult to remove. The soil will thus show a high water-holding capacity, so that the air-entry value of the soil will be increased. As the volumetric water content increases, the pore and connectivity state of the soil structure changes. Soil samples with higher dry densities contain more hydrophilic clay minerals and thus show strong hydrophilicity. Thus, the matric suction decreases more slowly.

Overall, the effect of the dry density on the SWCC can also be explained in terms of the change in the pore state of the soil [21]. Therefore, in our subsequent analysis of the EIS results, the equivalent circuit elements that characterize changes in the pores of the soil will be studied.

3.2.1 EIS results for the loess-like silt samples

The results of the EIS tests on loess-like silt samples with different dry densities are shown in Figs. 8–9, and different water contents are shown in Figs. 10–14 in the form of Nyquist and Bode diagrams. Areas of particular interest in these diagrams are shown in greater detail in the form of insets.

The test results show that the difference between the preset water content and actual water content is small in each case, so the preset water content values are used in the analysis of the EIS test results that follows.

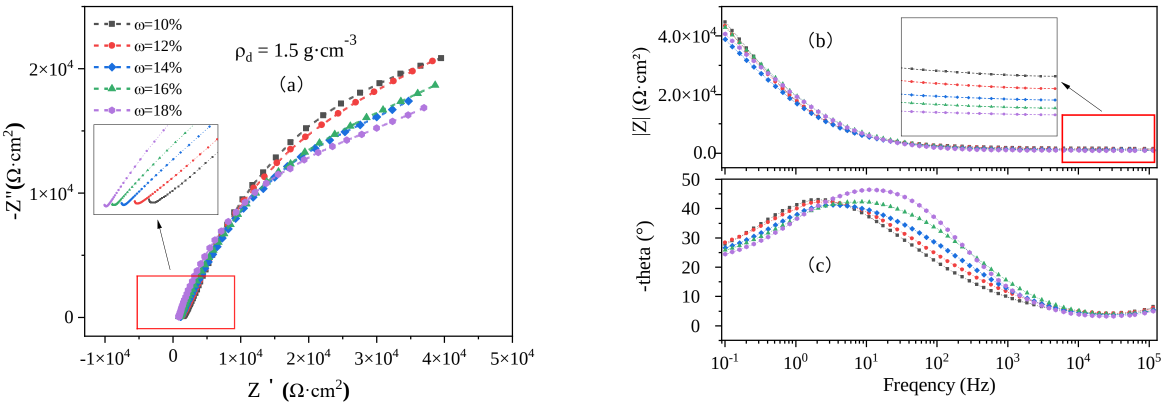

Figure 8. EIS results for loess-like silt with a dry density of 1.5 g·cm^{-3}.

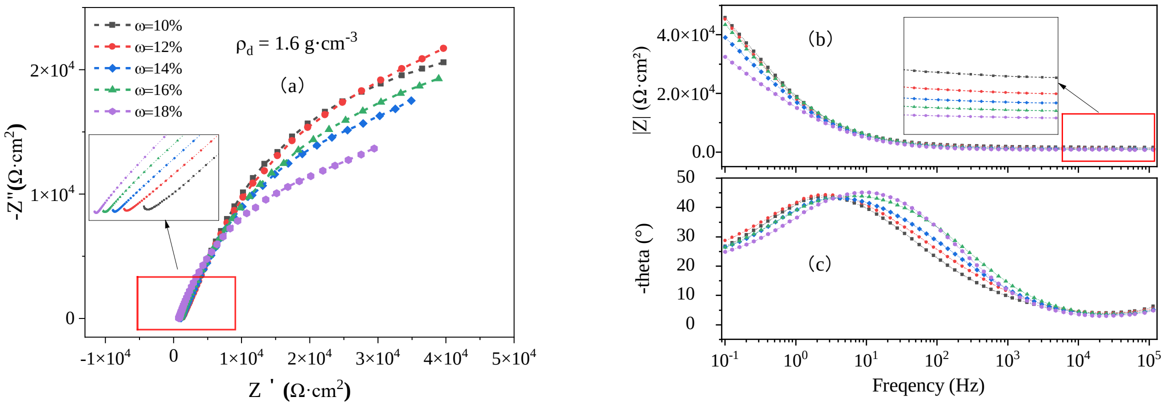

Figure 9. EIS results for loess-like silt with a dry density of 1.6 g·cm^{-3}.

Figs. 8 and 9 show the EIS results for soil samples with dry densities of 1.5 and 1.6 g·cm^{-3}, respectively. There are two capacitive reactance arcs in the Nyquist diagrams (Figs. 8a and 9a), one in the high-frequency region and the other in the low-frequency region. Correspondingly, there are two peaks in the Bode diagrams (Figs. 8c and 9c). These results indicate that the equivalent circuit model has two specific time constants. In addition, the phase angles at the peaks do not reach the critical value, indicating that the electrode surface is rough [33].

For a given dry density, as the water content increases, the intercept between the curve and the transverse coordinate in the Nyquist diagram gradually decreases, indicating that the impedance of the soil sample decreases. This is consistent with the results of Wang et al. [47], who showed that the impedance of a soil sample is inversely proportional to its water content. The Nyquist diagrams for samples with water contents of 16% and 18% show obvious diagonal characteristics compared with those with lower water content (10%, 12%, and 14%). This indicates that diffusion is making a contribution to the impedance (however, a 45° diagonal is not formed).

The trends in the two Bode diagrams in Figs. 8 and 9 are essentially the same. The modulus of the impedance |Z|, for example, gradually decreases as the frequency increases [34]. In the mid–high frequency range (10^2–10^5 Hz), the impedance curve is virtually horizontal implying that |Z| is approximately constant. As highlighted in the insets, at high frequency, the value of |Z| clearly decreases as the water content increases. The general trend in the phase angle plots is that the phase angle increases at first, then decreases, and then increases again as the frequency increases. The phase angle therefore exhibits a peak value in the low frequency range (10^{-1}–10^2 Hz). The frequency at which the peak occurs can also be seen to increase significantly as the water content increases.

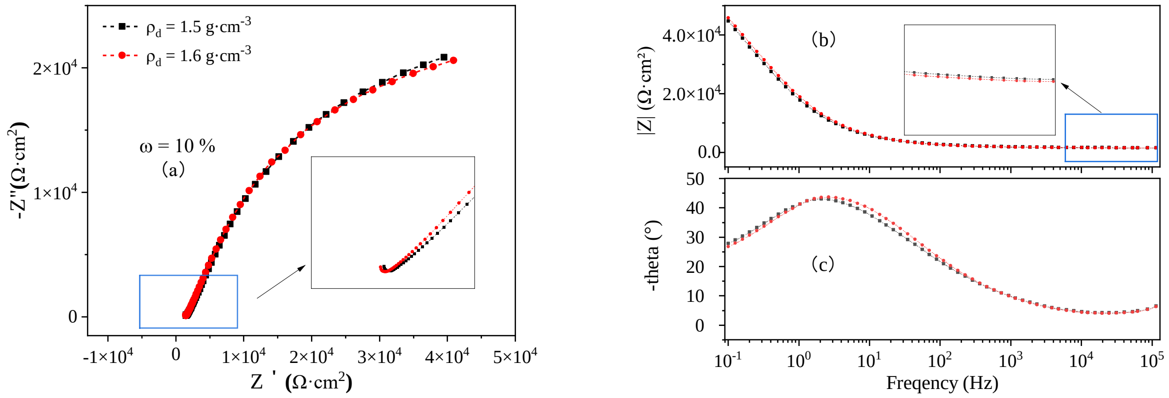

Figure 10. EIS results for loess-like silt with a water content of 10%.

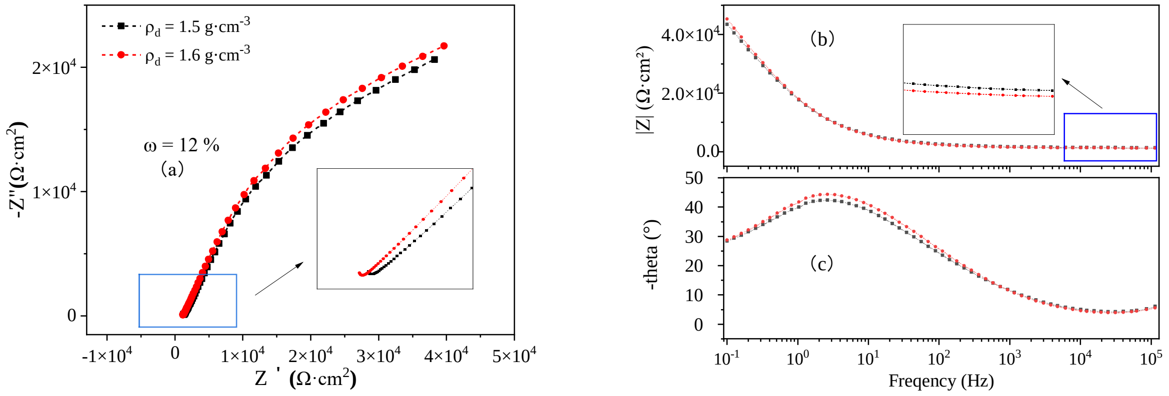

Figure 11. EIS results for loess-like silt with a water content of 12%.

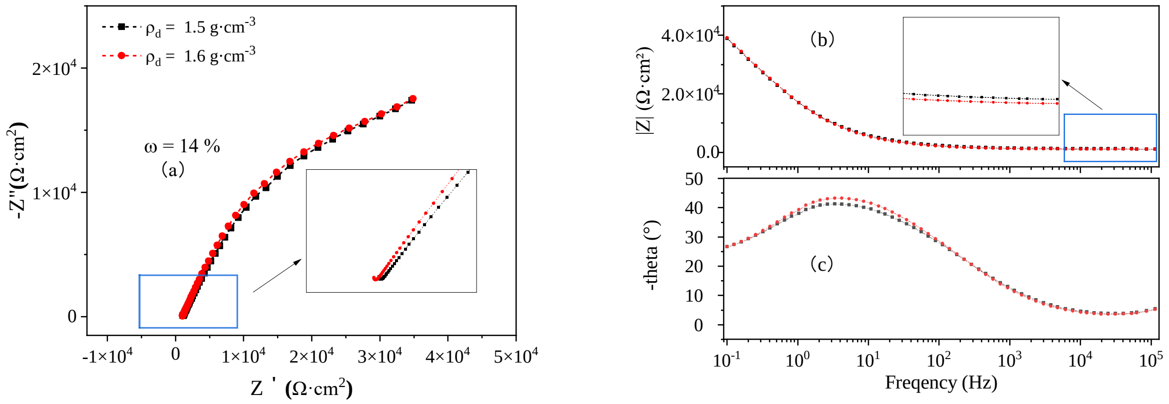

Figure 12. EIS results for loess-like silt with a water content of 14%.

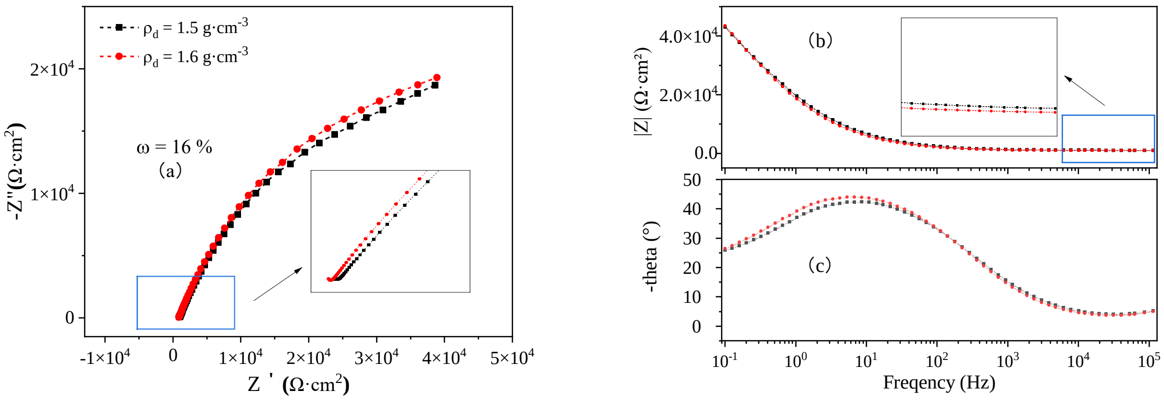

Figure 13. EIS results for loess-like silt with a water content of 16%.

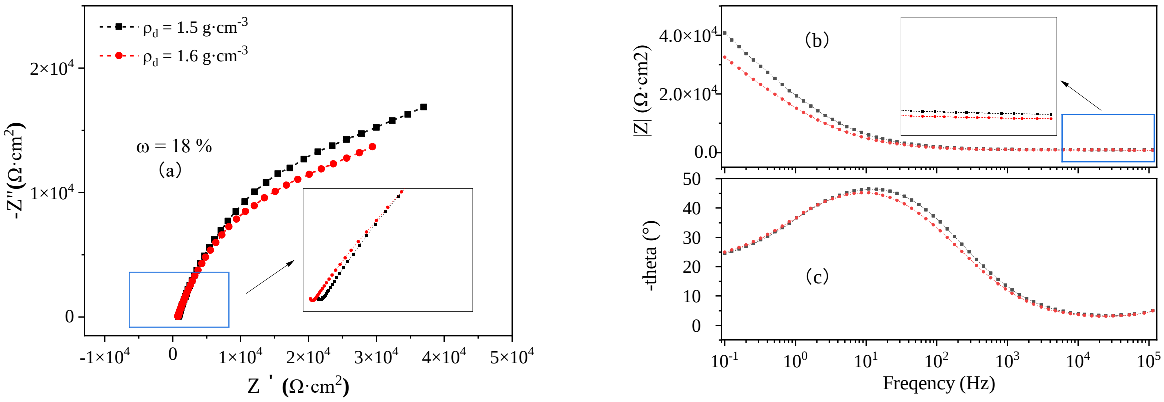

Figure 14. EIS results for loess-like silt with a water content of 18%.

The EIS results are replotted in Figs. 10–14 to make it easier to compare the responses of the soil samples with dry densities of 1.5 and 1.6 g·cm^{-3} for a given water content. As can be seen from the figures, the intercept between the curve in the Nyquist diagram and the real axis becomes smaller and smaller as the dry density increases, indicating that the impedance of the soil is decreasing [47]. The Bode diagrams (Figs. 10b–14b) also show that the |Z| values in the mid–high frequency region decrease as the dry density of the soil increases.

3.2.2 Equivalent circuit model for the loess-like silt

When the system is subjected to the AC disturbance signal, the main response is a three-step electrode reaction which occurs on the electrode surface. These involve a two-step mass transfer process and a one-step phase boundary reaction process [21]. According to Han et al. [37], the internal conductive paths in loess-like silt can be divided into three types (Fig. 15): (i) a discontinuous soil particle pore path (DSPP), (ii) a continuous soil particle path (CSP), and (iii) a continuous pore path (CPP). The frequency response of the whole circuit is generally not simple as it does not take the form of a simple composite or equivalent element (which is the result of the frequency response of each of its parts). Therefore, when establishing an equivalent EIS circuit, we should not rely just on the actual electrical processes taking place but also take into account the EIS characteristics of the actual soil.

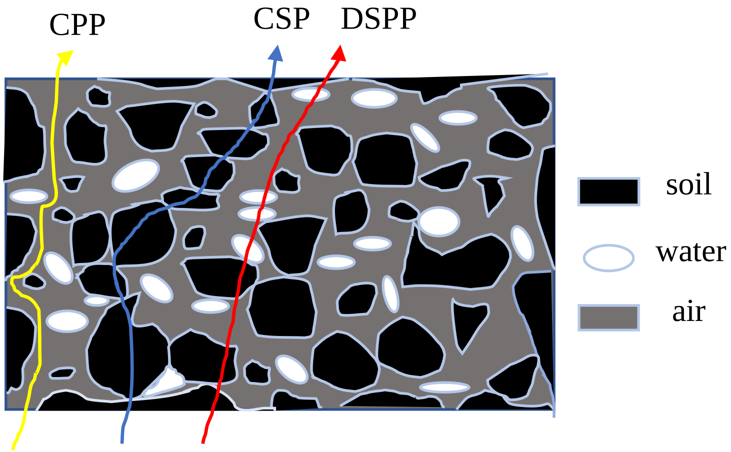

Figure 15. The internal conductive paths in loess-like silt.

In this work, we combine the conductive paths described by Han et al. [37] with the actual EIS characteristics determined experimentally (Figs. 8 and 9) to establish the equivalent circuit model. This approach allows us to investigate the physical meaning of each parameter in the model using the electrochemical software ZView2.

First, obvious diffusion characteristics are observed when the water content is 16%–18%. Therefore, two models need to be established: one to describe the response when the water content is 10%–14% and another when the water content is 16%–18% (Fig. 16). In Fig. 16, CPE represents a constant phase angle element. It takes the form of a double-layer capacitance and replaces the non-ideal state of the phase boundary reaction zone on the copper electrode surface in order to avoid the 'dispersion effect' [55]. Its impedance is represented by the double-layer capacitance parameter CPE-T and dispersion angle parameter CPE-P. The component labeled R_{ct} represents the charge transfer resistance of the phase boundary reaction zone on the copper electrode surface [56]; C_{csp} represents the double-layer capacitance formed on the surfaces of the continuous clay particles in the CSP path; C_{sp} represents the double-layer capacitance formed on the surfaces of the discontinuous clay particles in the DSPP path; R_{pp} represents the disconnected pore resistance in the DSPP path; R_{cpp} represents the connected pore resistance in the CPP path; and W represents a semi-infinite diffusion element (Warburg) [42]. In our tests, non-ideal Warburg behavior was observed so a CPE is used instead in order to achieve a better fitting effect.

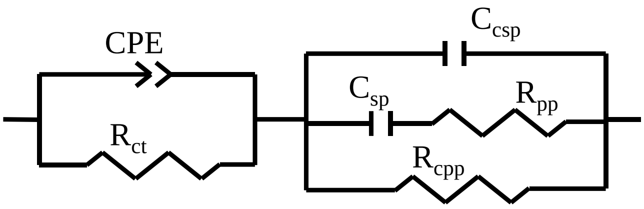

(a) $(CR_{ct})(C_{csp}(C_{sp}R_{pp})R_{cpp}))$

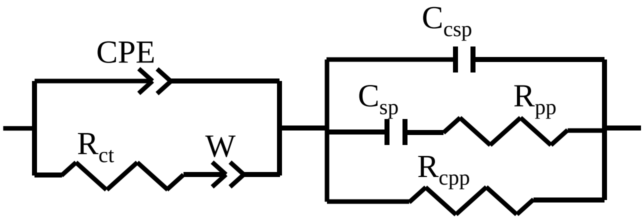

(b) $(C(R_{ct}W))(C_{csp}(C_{sp}R_{pp})R_{cpp}))$

Figure 16. Equivalent circuit models for soil containing: (a) 10%–14%, and (b) 16%–18% water content.

3.2.3 Fitting results

The EIS data gathered from the soil samples with different dry densities and water contents were fitted to the theoretical expressions describing the equivalent circuit models shown in Fig. 16. The fitting parameters thus derived are presented in Table 5. The deviation between the data and curve of best fit is generally less than 10%, on the whole.

Table 5. Parameter values obtained by fitting the EIS results (for loess-like silt samples with different dry densities and water contents) to the equivalent electrochemical circuit models.

ρ_d g·cm^{-3}	ω %	Rct Ω·cm^2	CPE$_1$-T S·cm^{-2}·s^{-n}	CPE$_1$-P n	Ccsp F·cm^{-2}	C$_{sp}$ F·cm^{-2}	R$_{cpp}$ Ω·cm^2	Rpp Ω·cm^2	CPE$_2$-T S·cm^{-2}·s^{-n}	CPE$_2$-P n
1.5	10	131500	2.809E-05	0.5051	1.02E-10	2.245E-05	9680	1785		
	12	122400	2.628E-05	0.5077	1.03E-10	2.369E-05	7197	1568		
	14	72930	2.079E-05	0.5469	1.02E-10	2.870E-05	2872	1757		
	16	566	1.090E-05	0.6115	4.72E-10	5.441E-05	2602	535	1.916E-05	0.1602
	18	546	7.048E-06	0.7092	4.85E-10	6.422E-05	1712	491	2.382E-05	0.1857
1.6	10	103600	2.421E-05	0.5315	1.04E-10	2.008E-05	8710	1780		
	12	96800	2.176E-05	0.5448	1.08E-10	2.484E-05	6008	1458		
	14	70130	2.057E-05	0.5651	1.08E-10	2.659E-05	3338	1478		
	16	440	1.210E-05	0.6223	4.04E-10	7.812E-05	2351	603	1.805E-05	0.1408
	18	406	1.051E-05	0.6864	4.11E-10	5.814E-05	1543	576	2.867E-05	0.1767

It can be seen from Table 5 that the way R_{cpp} changes is the same as the way the total pore resistance R due to R_{cpp} and R_{pp} changes. That is, R_{cpp} and the volume and number of connected pores in the soil can characterize the volume and number of total pores in the soil. For soil with a given dry density, R_{ct} decreases significantly as the water content is increased. This suggests that the phase boundary reaction zone is becoming progressively more filled with aqueous solution and thus increasing the conductivity of the path. Moreover, R_{ct} decreases precipitously at first and then much more slowly. That is, the effect of the increasing water content on R_{ct} becomes much weaker after the plastic limit is exceeded.

It can also be seen that the capacitance parameter CPE_1-T of CPE_1 decreases and CPE_1-P increases. That is, the ability of the sample to store charge decreases and the charge can be transferred more freely. As the water content increases, the system shows obvious signs of diffusion processes occurring. Overall, as the water content increases, R_{cpp} tends to decrease. The rate of decline is faster in the 10%–14% samples and much slower in the 14%–18% samples. This indicates that the increase in the water content makes the volume and number of interconnected pores in the soil decrease.

When the water content is 10%–12%, R_{cpp} is much larger than R_{pp}. This indicates that the volume and number of interconnected pores in the soil are large and that the soil particles do not easily make contact. As the water content increases, both R_{cpp} and R_{pp} decrease, indicating that the soil pores are becoming filled with water and the volume and number of pores are decreasing. However, when the water content is 14%, there is significant fluctuation in the R_{pp} value, indicating that some of the connected pores are becoming interrupted thus forming disconnected pores. This is because increasing the water content in the pores lubricates the soil particles and this allows better contact to be made between the soil particles.

As the water content continues to increase beyond the plastic limit, both R_{cpp} and R_{pp} continue to decrease. However, the decrease in the value of R_{cpp} is larger than that in R_{pp}, indicating that R_{cpp} is more sensitive to a change in water content. As the water content increases, C_{csp} and C_{sp} generally increase overall. This trend indicates that an increase in water content in the pores leads to more cations being attracted to the electric double layer formed by the soil particles. As a result, the thickness of the electric double layer decreases and the capacitance value increases.

Table 5 also shows that R_{ct} decreases as the dry density increases, indicating that it becomes easier for charge transfer to occur in the phase boundary reaction zone. Overall, the dry density also affects how R_{cpp} and R_{pp} vary with water content. When the water content is 10%–12%, R_{cpp} and R_{pp} decrease as the dry density increases, indicating that the volume and number of pores in the soil decrease. However, when the water content is 14%, R_{cpp} increases and R_{pp} decreases. This may be because the lubrication effect becomes more prominent due to the increased presence of aqueous solution. This allows the soil particles to be rearranged so that unconnected pores in the soil can be washed into new connected pores. The volume and number of unconnected pores in the soil thus decrease while the volume and number of connected pores increase. When the water content is 16%–18% (i.e. after the plastic limit is exceeded), R_{cpp} continues to decrease but to a lesser degree. This indicates that the volume and number of interconnected pores in the soil are still decreasing as the dry density increases. However, R_{pp} increases in a small range, which may be due to the lubrication effect of the water which causes the soil particles to be rearranged thus improving their contact. As a result, the distribution of the pores becomes more uniform, so that the connected pores in the soil are squeezed and washed into disconnected pores. Thus, the volume and number of disconnected pores increase to a certain extent.

The C_{sp} and C_{csp} values are very similar when the water content is 10%–14%. However, C_{csp} is much smaller than C_{sp} when the content is 16%–18%. This shows that the capacitance is also affected by mineral composition, pore structure, and water content [47]. Increasing the dry density increases the number of clay particles and the capacitance value. When the pore connectivity is poor, the electric double-layers are incomplete and the capacitance is small. Increasing the water content also increases the ion concentration, decreases the thickness of the double-layer, and increases the capacitance value. However, an excessive number of cations leads to the same charges being mutually excluded.

3.3 Relationship between electrochemical parameters and matric suction

In this work, the matric suction values in loess-like silt samples with different water contents and dry densities were determined together with EIS data. Our subsequent analysis shows that the electrochemical parameters R_{cpp} and R_{pp} can reflect the change in the pore characteristics of the unsaturated soil. The parameter R_{cpp} can also be used to characterize the change in the total pore resistance in the soil. Therefore, the relationship between R_{cpp} and matric suction can be established for samples with the same dry density.

For a particular dry density value, R_{cpp} decreases as the water content increases. The decline in R_{cpp} value is rapid in the early stages and slower in the later stages. The matric suction exhibits the same variational trend. For soil samples with the same water content, the matric suction and connected pore resistance R_{cpp} were also found to be sensitive to the dry density when the water content is low. When the water content is low, the volume and number of connected pores in the soil with high dry density are small and the matric suction is also small. However, as the water content increases, the number of connected pores increases and then decreases and the matric suction is mainly affected by the mineral composition. Hence, the matric suction of the soil with high dry density is larger than low dry density. Therefore, this experiment establishes the relationship between R_{cpp} and matric suction (for soil with the same dry density and different water contents).

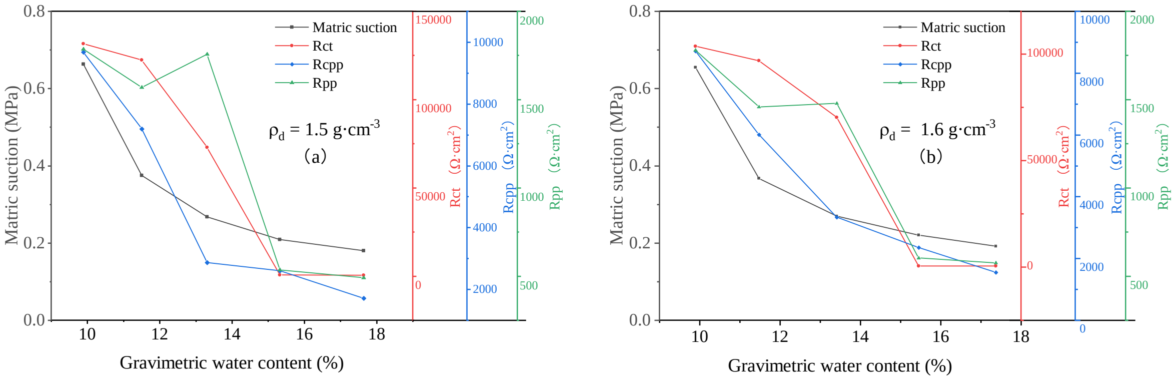

Figure 17. Variation of the matric suction, Rct, Rcpp, and Rpp with water content for loess-like silt samples with dry densities of: (a) 1.5 $g\cdot cm^{-3}$ and (b) 1.6 $\cdot gcm^{-3}$.

Fig. 17 shows how the matric suction and R_{ct}, R_{cpp}, and R_{pp} parameters vary with water content in loess-like silt samples with different dry densities. It can be seen from these graphs that the matric suction and R_{cpp} parameter behave very similarly as the water content increases. That is, as the water content increases, the matric suction and R_{cpp} values decrease continuously. The relationship between these two parameters can be illustrated more clearly by plotting scatter diagrams and mathematically calculating the degree of correlation between them, as shown in Fig. 18. As can be seen, the matric suction and R_{cpp} parameter are significantly and positively linearly correlated (the correlation coefficients, R^2, are both greater than 0.90 for the two cases illustrated, showing that the fitting accuracy is good).

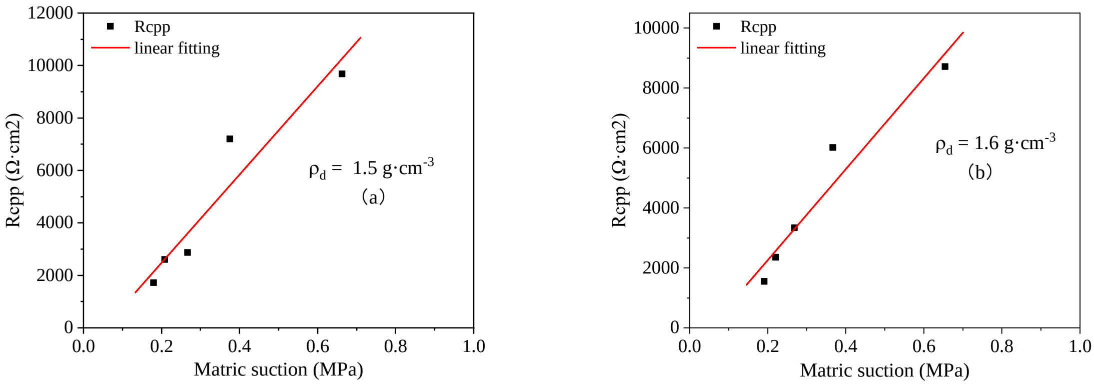

Figure 18. Correlation between matric suction and Rcpp parameter for the loess-like silt.

Therefore, a change in matric suction can be directly related to the corresponding change in R_{cpp}. Overall, the smaller the R_{cpp} value, the lower the matric suction and the higher the water content. This is because, as the water content is increased, the volume and number of total pores in the soil decrease. As a result, the total volume and number of connected pores (which account for a large proportion of the total) also decrease. The decrease in pore volume and number will affect the soil–water interaction area and shape of the contraction film. Consequently, the radius of curvature of the bending surface in the soil pores decreases as does the water-holding capacity of the soil. Hence, the matric suction also decreases.

4. CONCLUSIONS

In this paper, an electrochemical workstation and a chilled-mirror dew-point meter were used to determine the total suction, osmotic suction, and electrochemical impedance spectra of loess-like silt samples with different initial water contents and initial dry densities. The data were used to generate soil water characteristic curves and the variation of the matric suction was analyzed. Equivalent circuit models were established for the soil and the physical meaning of the electrochemical elements in the models analyzed. The data were also fitted to generate SWCC. The way the matric suction changes with the water content and dry density was analyzed. The relationships between the electrochemical parameters and matric suction were then explored. The main conclusions of the work are as follows.

(1) The water content and dry density of the soil significantly affect the matric suction therein. As the water content increases, the matric suction decreases. The variation of the matric suction with dry density is also affected by the water content. When the water content is low, the soil with the smaller dry density has the larger matric suction; when the water content is high, the matric suction is smaller in the soil with lower dry density.

(2) The water content and dry density of the soil significantly affect its electrochemical properties. For soil samples with the same dry density, the charge transfer resistance (R_{ct}) and connected pore resistance (R_{cpp}) decrease as the water content increases. As the dry density increases, the charge transfer resistance (R_{ct}) decreases.

(3) The effect of the water content on the matric suction in the unsaturated loess-like silt can be characterized by the connected pore resistance (R_{cpp}). For samples with the same dry density, R_{cpp} and matric suction are linearly and positively correlated. That is, as the water content changes, the R_{cpp} and matric suction values change in the same direction.

ACKNOWLEDGEMENTS

The present work is supported by the National Natural Science Foundation of China (No:41807256), the Applied Basic Research Program in Shanxi Province (No. 20210302123139), the Science and Technology Innovation Project of Colleges and Universities in Shanxi Province (NO.2019L1260).

References

1. Y. B. Guan, S. T. Yang, C. S. Zhao, H. Z. Lou, K. Chen, C. B. Zhang, and B. W. Wu, *Soil Tillage Res.*, 205 (2021) 104800.
2. L. N. Yuan, L. Li, T. Zhang, L. Q. Chen, W. Q. Liu, S. Hu, and L. H. Yang, *ISPRS Int. J. Geo-Inf.*, 10 (4) (2021) 233.
3. H. Zheng, X. A. Li, Y. H. Deng, J. Li, and F. Wen, *Water*, 14 (9) (2022) 1344.
4. W. L. Xie, Q. Y. Guo, J. Y. Wu, P. Li, H. Yang, and M.S. Zhang, *Nat. Hazards*, 106 (1) (2021) 805-827.
5. D. Y. Xie, *Yen T'u Kung Ch'eng Hsueh Pao*, 23 (1) (2001) 3-13.
6. S. Dong, H. Y. Wang, J. Li, F. L. Ma, and X. H. Bai, *J. Guangxi Univ. (Nat. Sci. Ed.),* 45 (5) (2020) 978-985.
7. C. X. Huang, M. Huang, W. Cai, G. X. Chen, C. Liu, and Y. M. Zhang, *Yen T' u Kung Ch' eng Hsueh Pao*, 42 (4) (2020) 758-764.
8. Y. R. Zhao, X. J. Li, P. Tai, L. P. Huang, B. Pu, and R. Chen, I*nt. J. Numer. Anal. Methods Geomech.*, 46 (7) (2022) 1224-1240
9. J. Xu, Z. Wang, and W. X. Li, *Yen Shih Li Hsueh Yu Kung Ch' eng Hsueh Pao,* z1 (2000) 905-909.
10. J. J. Fang, Y. X. Feng, and S. J. Shao, *Rock Soil Mech.*, 38 (9) (2017) 2597-2604.
11. J. Feng, and G. Z. Zhang, *Geofluids*, 2021 (2021), doi: 10.1155/2021/5475391.
12. Y. Wang, T. L. Li, C. X. Zhao, X. K. Hou, P. Li, and Y. G. Zhang, *Environ. Earth Sci.*, 80 (22) (2021) 1-12.
13. B. F. Cao, Y. K. Tian, R. Gui, and Y. Liu, *Front. Environ. Sci.*, 9 (2021) 286.
14. W. Liu, G. Q. Cai, J. Li, and C. G. Zhao, *Yen T' u Kung Ch' eng Hsueh Pao*, 43 (3) (2021) 547-555.
15. H. Zhong, G. T. Zhao, J. G. Lin, K. W. Fan, and W. L. Zou, *Eng. Geol.*, 297 (2022) 106533.
16. Y. P. Nie, W. K. Ni, X. N. Li, H. M. Wang, K. Z. Yuan, Y. X. Guo, and W. X. Tuo, *Water*, 13 (13)

(2021) 1809.
17. Y. Wang, T. L. Li, P. Li, Y. L. Lei, and D. D. Lawrence, *Adv. Civ. Eng.*,2021 (2021), doi: 10.1155/2021/6689680.
18. J. H. Shen, M. J. Hu, X. Wang, C. Y. Zhang, and D. S. Xu, *Front. Environ. Sci.*, 9 (2021) 303.
19. W. L. Zou, X. Q. Wang, F. D. Luo, J. F. Zhang, Y. X. Ye, and Z.W. Hu, *Yen T' u Kung Ch' eng Hsueh Pao*, 39 (9) (2017) 1711-1717.
20. H. E. Chen, J. F. Li, X. Q. Yuan, B. Shi, and W. C. Shan, *Bull. Eng. Geol. Environ.*, 80 (11) (2021) 8535-8551.
21. Y. L. Chen, and T. UCHIMURA, *J. Cent. South Univ. (Sci. Technol.)*, 48 (3) (2017) 813-819.
22. G. L. Tao, K. Gu, C. H. Zhong, Y. Y. Chen, D. Lei, and Z. Y. Li, *Arab. J. Geosci.*, 14 (23) (2021) 1-14.
23. F.Y. Zhang, C. X. Zhao, S. D. N. Lourenco, S. M. Dong, and Y. Jiang, *Bull. Eng. Geol. Environ.*, 80 (1) (2021) 717-729.
24. S. Rajesh, and V. Khan, *Appl. Clay Sci.*, 157 (2018) 177-188.
25. G. L. Tao, Y. Y. Chen, H. L. Xiao, Y. Chen, and W. Peng, *Adv. Mater. Sci. Eng.*, 2020 (2020), doi:10.1155/2020/1970314.
26. F. P. le Roux, and S. W. Jacobsz, *Geotech. Test. J.*, 44 (4) (2021) 1079-1096.
27. S. Rajesh, S. Roy, and S. Madhav, *Int. J. Geotech. Eng.*, 11 (4) (2017) 321-331.
28. N. Lu, *J. Geotech. Geoenviron. Eng.*, 146 (5) (2020) 02520001.
29. F. S. Cha, S. Y. Liu, Y. J. Dun, and K. R. Cui, *Rock Soil Mech.*, 31 (3) (2010) 1003-1008.
30. P. H. Lu, Y. He, Z. Zhang, and W. M. Ye, *Comput. Geotech.*, 138 (2021) 104360.
31. D. Gallipoli, and A. W. Bruno, *Acta Geotech.*, 17 (3) (2022) 819-835.
32. R.Z. Xie, P. J. Han, X. Y. Wang, B. Q. Li, B. He, F. L. Ma, and X. H. Bai, *Int. J. Electrochem. Sci.*, 15 (2020) 3543-3562.
33. Z.W. Chen, P. J. Han, B. He, F. N. Sun, X. L. Bai, X.Y. Wang, T. T. Guo, and X.Y. Wang, *Int. J. Electrochem. Sci.*, 16 (2021) 210914
34. S. Q. Peng, F. Wang and L. Fan, *Int. J. Electrochem. Sci.*, 14 (2019) 8611-8623.
35. F. Qin, C.L. Jiang, X.H. Cui, Q. Wang, J.H. Wang, R. Huang, D.T. Yu, Q. Qu, Y. J. Zhang, and P.D. Peng, *Int. J. Electrochem. Sci.*, 13 (2018) 1603-1613.
36. R. Z. Xie, Y. T. Xie, B. Q. Li, P. J. Han, B. He, B. J. Dou, and X. H. Bai, *Int. J. Electrochem. Sci.*, 16 (211211) (2021) 2.
37. P. J. Han, Y. F. Zhang, Y. F. Chen, and X. H. Bai, *J. Cent. South Univ.*, 22 (11) (2015) 4318-4328.
38. Z. W. Chen, P. J. Han, B. He, F. N. Sun, X. L. Bai, X. Y. Liu and Y. T. Wang, *Int. J. Electrochem. Sci.*, 16 (8) (2021).
39. P. Han, P. J. Han, Y. B. Yan, and X. H. Bai, *Int. J. Electrochem. Sci.*, 13 (11) (2018) 10548-10563.
40. Ž. Z. Tasić, M. B. P. Mihajlović, M. B. Radovanović, A. T. Simonović, and M. M. Antonijević, *J. Mol. Struct.*, 1159 (2018) 46-54.
41. Ž. Z. Tasić, M. B. P. Mihajlović, M. B. Radovanović, and M. M. Antonijević, *J. Mol. Liq.*, 265 (2018) 687-692.
42. Z. Z. Tasić, M. B. P. Mihajlović, A. T. Simonović, M. B. Radovanović, and M. M. Antonijević, *Sci. Rep.*, 9 (1) (2019) 1-14.
43. H. S. Magar, R. Y. Hassan, and A. Mulchandani, *Sensors*, 21 (19) (2021) 6578.
44. W. Choi, H. C. Shin, J. M. Kim, J. Y. Choi, and W. S. Yoon, *J. Electrochem. Sci. Technol*, 11 (1) (2020) 1-13.
45. C. Soares, J. T. Machado, A. M. Lopes, E. Vieira, and C. Delerue-Matos, *Food Chem.*, 302 (2020) 125345.
46. J. Li, R. Z. Xie, P. J. Han, and X. H. Bai, *Int. J. Electrochem. Sci.*, 15 (2020) 6227-6237.
47. S. Wang, and P. J. Han, *China Sciencepap.*, 2015 (18) 2169-2173.
48. A. Saha, and S. Sekharan, *J. Hydrol.*, 596 (2021) 126113.
49. M. T. Van Genuchten, *Soil Sci. Soc. Am. J.*, 44 (5) (1980) 892–898.

50. G. Q. Cai, B. W. Han, Y. Yang, W. Liu, and C. G. Zhao, *Yen T' u Kung Ch' eng Hsueh Pao*, 42 (S1) (2020) 11-15.
51. X. W. Liu, L. J. Chang, and X.R. Hu, *Rock Soil Mech.*, 30 (11) (2009) 3302-3306.
52. S. K. Vanapalli, D. G. Fredlund, D. E. Pufahl, and A. W. Clifton, *Can. Geotech. J.*, 33 (3) (1996) 379-392.
53. J. J. Fang, Y. X. Feng, and S. J. Shao, *Rock Soil Mech.*, 38 (09) (2017) 597-2604.
54. L. Wang, F. Y. Liu, and Z. Zhang, *Chan Chieh*, 46 (5) (2021) 147-150,163.
55. F .N . Sun, R. Z. Xie, B. He, Z.W. Chen, X. L. Bai, and P. J. Han, *Int. J. Electrochem. Sci.*, 16 (2021) 150878.
56. Y .J . Lan, H. L. Chang, G. Qi, P. J. Han, and B. He, *Int. J. Electrochem. Sci.*,16 (9) (2021).